Plasma Sources Sci. Technol. 33 (2024) 025010 (13pp)

https://doi.org/10.1088/1361-6595/ad2117

# Spatio-temporal electric field distributions in an atmospheric plasma jet impinging on a microchannel array surface

S Raskar<sup>1,\*</sup>, I V Adamovich<sup>1,\*</sup>, K Konina<sup>2</sup> and M J Kushner<sup>2</sup>

E-mail: raskar.1@osu.edu and adamovich.1@osu.edu

Received 20 October 2023, revised 28 December 2023 Accepted for publication 22 January 2024 Published 9 February 2024



### **Abstract**

The electric field distribution in the ionization waves (IWs) propagating over a microchannel array dielectric surface, with the channels either empty or filled with distilled water, is measured by ps electric field induced second harmonic generation. The surface IW is initiated by the atmospheric pressure  $N_2$ –Ar plasma jet impinging on the surface vertically and powered by ns pulse discharge bursts. The results show that the electric field inside the microchannels, specifically its horizontal component, is enhanced by up to a factor of 2. The field enhancement region is localized within the channels. The vertical electric field inside the channels lags in time compared to the field measured at the ridges, indicating the transient reversal of the IW propagation direction across the channels (toward the jet). This is consistent with the phase-locked plasma emission images and confirmed by the kinetic modeling predictions, which show that the IW 'jumps' over the empty channels and propagates into the channels only after the jump between the adjacent ridges. When the channels are filled with water, the wave speed increases by up to 50%, due to the higher effective dielectric constant of the surface. No evidence of a significant electric field enhancement near the dielectric surface (ceramic or water) has been detected, within the spatial resolution of the present diagnostic,  $\sim 100~\mu m$ .

Supplementary material for this article is available online

Keywords: electric field induced second harmonic generation (EFISH), microchannel surface, plasmas and liquids, atmospheric pressure plasma jets

Original content from this work may be used under the terms of the Creative Commons Attribution 4.0 licence. Any further distribution of this work must maintain attribution to the author(s) and the title of the work, journal citation and DOI.

<sup>&</sup>lt;sup>1</sup> Nonequilibrium Thermodynamics Laboratories, Department of Mechanical and Aerospace Engineering, The Ohio State University, Columbus, OH 43210, United States of America

<sup>&</sup>lt;sup>2</sup> Department of Electrical Engineering and Computer Science, University of Michigan, Ann Arbor, MI 48109, United States of America

<sup>\*</sup> Authors to whom any correspondence should be addressed.

## 1. Introduction

Streamers and ionization waves (IWs) propagating over the dielectric surfaces in atmospheric pressure plasmas have been detected in many types of electric discharges, including surface dielectric barrier discharges and atmospheric pressure plasma jets (APPJs), powered by AC waveforms and nanosecond pulses [1-4]. These waves have also been observed in plasmas propagating over the liquid surfaces [5, 6]. IWs propagating over the surfaces with complex morphology are of particular interest, since surface structures may enhance the electric field and electron temperature in the wave front and result in the localized generation of excited species and radicals [7]. One example of such surface is human skin, with microscale recesses such as pores and hair follicles. Quantitative understanding and predictive modeling of plasma interaction with such complex surfaces are critical for the development of biomedical applications of low-temperature plasmas. Unfortunately, surfaces with complex morphology may not be readily accessible to plasma characterization, and specifically to laser diagnostics. For this, simpler geometry textured surfaces, with arrays of microscale wells or channels which provide optical access, may be used. Microchannel array surfaces with the channels filled with water or aqueous solutions provide an additional perspective, since they can be used for the efficient and controlled plasma-assisted activation of water. Characterization of plasmas propagating over the microchannel surfaces will also provide the data for the validation of the kinetic models [7, 8], which may then be exercised to predict the plasma parameters for more complex surfaces, not readily accessible for the experimental diagnostic study.

The objective of the present work is to obtain an extensive set of data on the temporal and spatial distribution of the electric field components in a plasma jet impinging on a microchannel surface, using ps electric field induced second harmonic (EFISH) diagnostic [9, 10]. This approach makes possible the electric field measurements in proximity to the surface, down to  $\sim 100 \ \mu m$ , limited by the diameter of the focused laser beam. Recently, EFISH has been used extensively for the plasma jet characterization [10-13]. Ideally, these measurements could be done using a quasi-two-dimensional jet generating a 'curtain-like' effluent plasma [11], impinging on a plane surface with microchannels. However, this geometry would limit the optical access to the plasma within the channels, because of the laser beam clipping on the channel bottom and walls. This difficulty may be circumvented by using a curved dielectric surface, such as a cylinder with microchannels machined into the surface. In this case, the microchannels may also be easily filled with water, using the capillary forces, such that the same approach may be used to measure the electric field over the water filled channels and the 'ridges' between them.

Although EFISH offers high sensitivity, temporal resolution, and spatial resolution across the laser beam, its main disadvantage is the low spatial resolution along the pump laser beam, caused by the coherent signal growth in the beam direction. Additional difficulty of placing the EFISH signal on the absolute scale include the prediction of the coherent growth of the signal in the beam direction, which would require the prior knowledge of the electric field distribution [14]. However, this effect can be reduced by increasing the beam Rayleigh range and probing small-size plasmas. The use of the two-beam spatially enhanced EFISH (SEEFISH) [15], which has higher spatial resolution, is not feasible at the present conditions, due to the significantly lower signal.

The results of the present work, specifically the timeresolved plasma emission images and the electric field distributions, are compared briefly here with the two-dimensional (2D) plasma hydrodynamic simulations and more extensively in a companion paper [16], to provide additional insight into the underlying kinetics.

# 2. Description of experiment and model

## 2.1. Experimental

The experimental setup used in the present study is shown in figure 1. An atmospheric pressure plasma jet is sustained in a 10% N<sub>2</sub>-Ar mixture, with a co-flow of nitrogen, by repetitive bursts of high-voltage, ns duration pulses. The plasma jet apparatus, described in greater detail in [17], includes a 2 mm inside diameter quartz tube with a tungsten needle high voltage electrode inside and a grounded copper ring electrode outside, placed within a 9.5 mm inside diameter polycarbonate plastic tube, as shown schematically in figure 1. The flow rates of the N2-Ar mixture (through the quartz tube) and N2 co-flow (through the plastic tube) are 7 slm and 5 slm, respectively. The mixture composition and the flow rates are selected to generate a stable and diffuse plasma jet at the exit of the tube, without filamentation. The jet assembly is positioned 0.8 mm above the target dielectric surface, placed within a Petri dish 10 cm diameter and 1 cm deep (see figure 1). The target surface is a Macor ceramic tube 12.7 mm outside diameter, with an array of rectangular cross section channels  $(0.25 \text{ mm} \times 0.25 \text{ mm})$  machined into the surface, spanning a 23 mm interval. A grounded stainless-steel tube, 9.5 mm in diameter, is placed within the ceramic tube. The Petri dish can be partially filled with distilled deionized water, to the level several mm below the top of the ceramic tube. The water level in the dish is maintained using a syringe. In this case, the channels machined into the ceramic tube become filled with water, due to the capillary action, as shown in figure 1. Based on the water surface images and plasma emission images, the water surface appears steady in time. The discharge pulse duration  $(\sim 100 \text{ ns})$  is much shorter compared to the characteristic time scale of the liquid motion. Also, no liquid motion on a longer time scale (from  $\sim 1$  s to  $\sim 1$  h) has been detected, in spite of the gradual evaporation of the water in the Petri dish.

During the experiments, the plasma jet is impinging on the microchannel array Macor ceramic surface, with the channels dry or filled with water. The plasma is sustained by the negative polarity bursts, 10 pulses/burst, pulse repetition rate 10 kHz. Typical voltage and current pulse waveforms, with

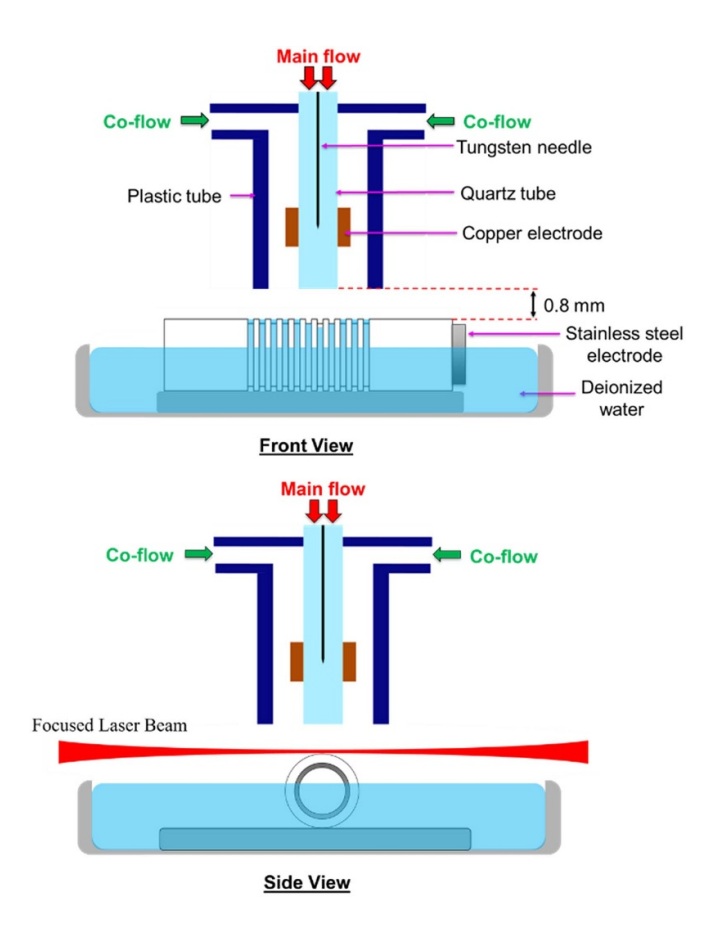


**Figure 1.** Schematic of the atmospheric pressure plasma jet impinging on a microchannel array Macor ceramic surface: (a) front view, with the microchannels filled with water; (b) side view, showing the focused laser tangent to the Macor surface.

peak voltage of 8.4 kV, voltage pulse duration approximately 100 ns FWHM, and peak current of 0.48 A, are shown in figure 2. The burst repetition rate is maintained at 10 Hz, to match the repetition rate of the pump laser, used to measure the electric field in the plasma by the EFISH generation. The EFISH diagnostic used in the present work is the same as in [11]. Briefly, the fundamental 1064 nm output of an Ekspla SL333 ps Nd: YAG laser (pulse duration 150 ps, energy 2 mJ/pulse) is focused in the plasma jet using a 20 cm focal distance lens, as shown schematically in figure 1, and used as a pump beam. A long pass filter placed after the focusing lens blocks the stray second harmonic signal. The EFISH signal beam generated in the plasma is collimated, separated from the pump beam by a pair of dichroic mirrors and a dispersion prism, and focused on the PMT detector monitored by an oscilloscope. A narrow band pass filter in front of the PMT discriminates the stray light, and a polarizer in a rotation mount isolates the signal generated by a particular component of the electric field. The PMT gain is kept low to limit saturation at high peak electric field values. The laser pulse energy is monitored by a photodiode.

The entire plasma jet/Petri dish assembly, mounted on a 3D translation stage, can be moved relative to the laser beam, for the spatially resolved electric field measurements. The

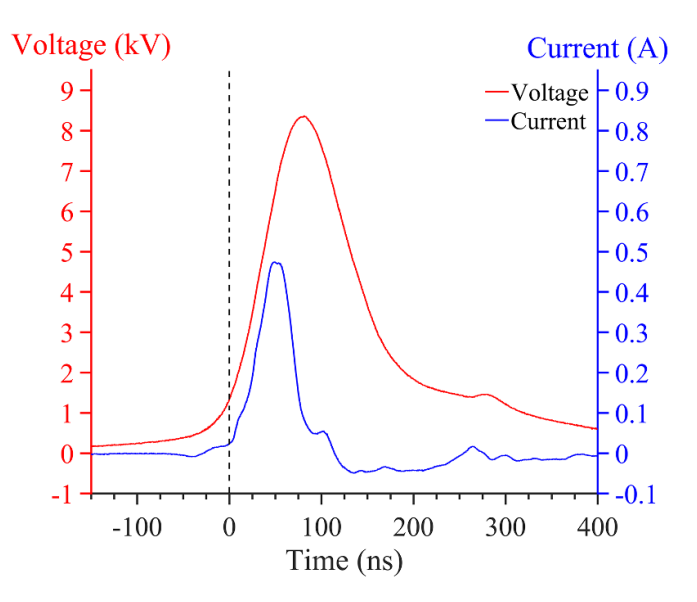


**Figure 2.** Negative polarity pulse voltage and current waveforms, with t=0 corresponding to the sudden rise of the discharge current (breakdown moment). The voltage and current polarity are inverted. The waveforms for plasmas over dry and water-filled channels are very similar.

time-resolved electric field is measured by varying the delay between the last discharge pulse in the burst and the laser pulse. The raw EFISH signal waveforms acquired during the individual laser shots are placed into the 'time bins' 2 ns long, arranged according to the laser pulse delay time relative to the last discharge pulse (20–180 ns), and analyzed during the data post-processing. The size of the bins determines the temporal resolution of the data, and the number of signal waveforms in the bins (typically 50–100) is determined by the total number of laser shots during a single run (6000). No averaging of the signal is performed during the experiments. During the data post-processing, the mean value and the standard deviation of the signal are determined for every bin, and the calibration is applied to the mean values to put them on the absolute scale. For every time bin, the standard deviation of the mean signal accumulated over 50–100 discharge bursts does not exceed ≈10%, indicating good burst-to-burst reproducibility of the time-resolved data. The use of a cylindrical, rather than plane, target surface, makes possible positioning the laser beam closer to the surface, without clipping the laser beam. The curvature radius of the surface, 6.35 mm, is much greater compared to the width and depth of the microchannels (0.25 mm), such that it is unlikely to affect the measurement

The diameter of the laser beam at the focal point (beam waist), attenuated to 0.2 mJ/pulse by a half wave plate/polarizing beam splitter combination, is measured by scanning the beam across a knife edge. The  $1/e^2$  Gaussian beam diameter inferred from these measurements is  $w_0 = 102 \pm 6 \mu m$ . The same approach has been used to determine the laser beam position relative to the ceramic surface. The beam center was placed approximately 70  $\mu m$  from the surface, as shown

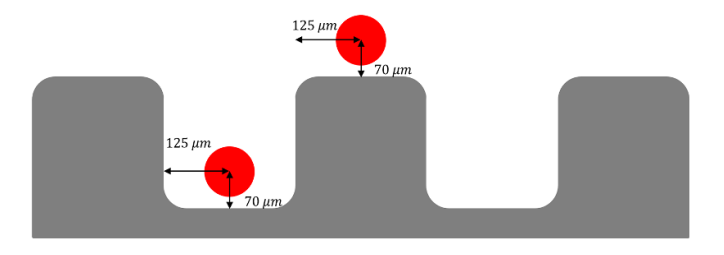
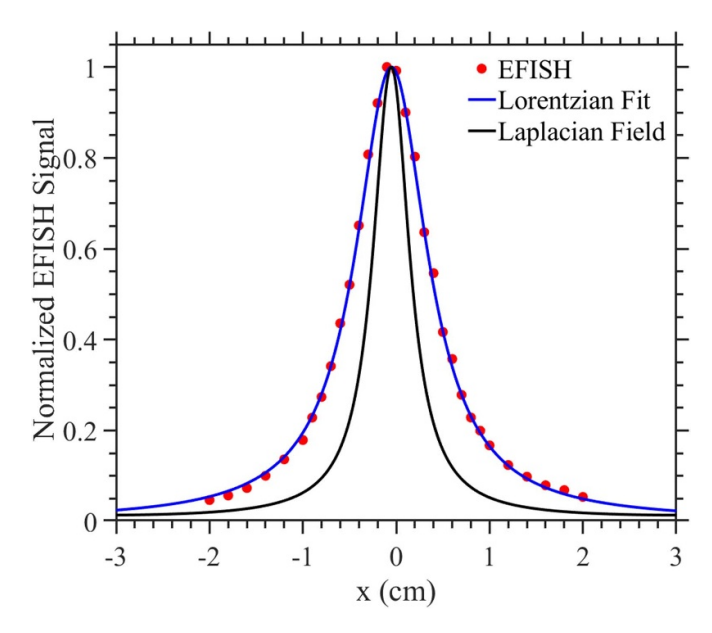


Figure 3. Schematic of the laser beam positions inside and outside of the microchannels.



**Figure 4.** Spatial distribution of the EFISH Signal, measured by traversing a pair of parallel cylindrical electrodes along the laser beam and plotted along with the normalized Laplacian field distribution.

schematically in figure 3,  $10~\mu m$  away from the onset of the detectable reduction of the transmitted laser pulse energy clipped by the surface. The spatial resolution of the EFISH diagnostic in the direction of the laser beam was quantified by traversing a pair of biased parallel cylindrical rod electrodes 1.6 mm in diameter in ceramic sleeves placed 5.4 mm apart, as in our previous work [15]. The normalized EFISH signal is plotted along with the Laplacian field distribution between the electrodes in figure 4, indicating that the present diagnostic does not fully resolve the electric field profile, yielding the signal FWHM of 10~mm, compared to 6~mm for the Laplacian field (see figure 4).

The electric field measured in the plasma jet is placed on the absolute scale by measuring the EFISH signal generated by the Laplacian field, produced by applying the high voltage to both of the plasma jet electrodes (the needle and the ring). The 2D distribution of the vertical component of the electric field in the plane of symmetry of the plasma jet, predicted by solving the Laplace equation, is plotted in figure 5(a). Figure 5(b) shows the vertical electric field profile along the laser beam, when it is tangent to the ceramic surface, with the FWHM of approximately 12 mm. The EFISH signal measured at these conditions, for different values of the applied voltage, is correlated to the peak electric field in the gap predicted by

the Laplace equation solver. Figure 5(c) shows the sample calibration curves (peak vertical Laplacian electric field vs. the applied pulse peak voltage) measured at several different spanwise locations along the microchannel surface. Similar calibration curves, both for the vertical and horizontal components of the Laplacian field, have been obtained at every measurement location along the surface (16 total). The use of different calibration curves for different locations is necessary because the composition of the plasma varies along the surface, as the N<sub>2</sub>-Ar plasma jet is mixing with the nitrogen co-flow, ambient air, and water vapor. The nonlinearity apparent in the calibration curves is due to the partial saturation of the PMT at high electric field values. Although the non-linearity can be removed by reducing the PMT gain, operating at high gain provides a wider range of electric fields that can be measured with high signal-to-noise.

For the field measurements outside the calibration range, we used composite calibration curves, obtained for the same range of Laplacian fields but using two different laser pulse energies. It was verified that in the linear PMT regime, the ratio of the square roots of EFISH signals at the same field is equal to the laser intensity ratio, i.e.  $\frac{\sqrt{S_2(E,I_2)}}{\sqrt{S_1(E,I_1)}} = \frac{I_2}{I_1}$ . This indicates that the square root signals are equal when the product of the electric field and laser intensity is the same, i.e.  $\sqrt{S(E_2,I_2)} =$ 

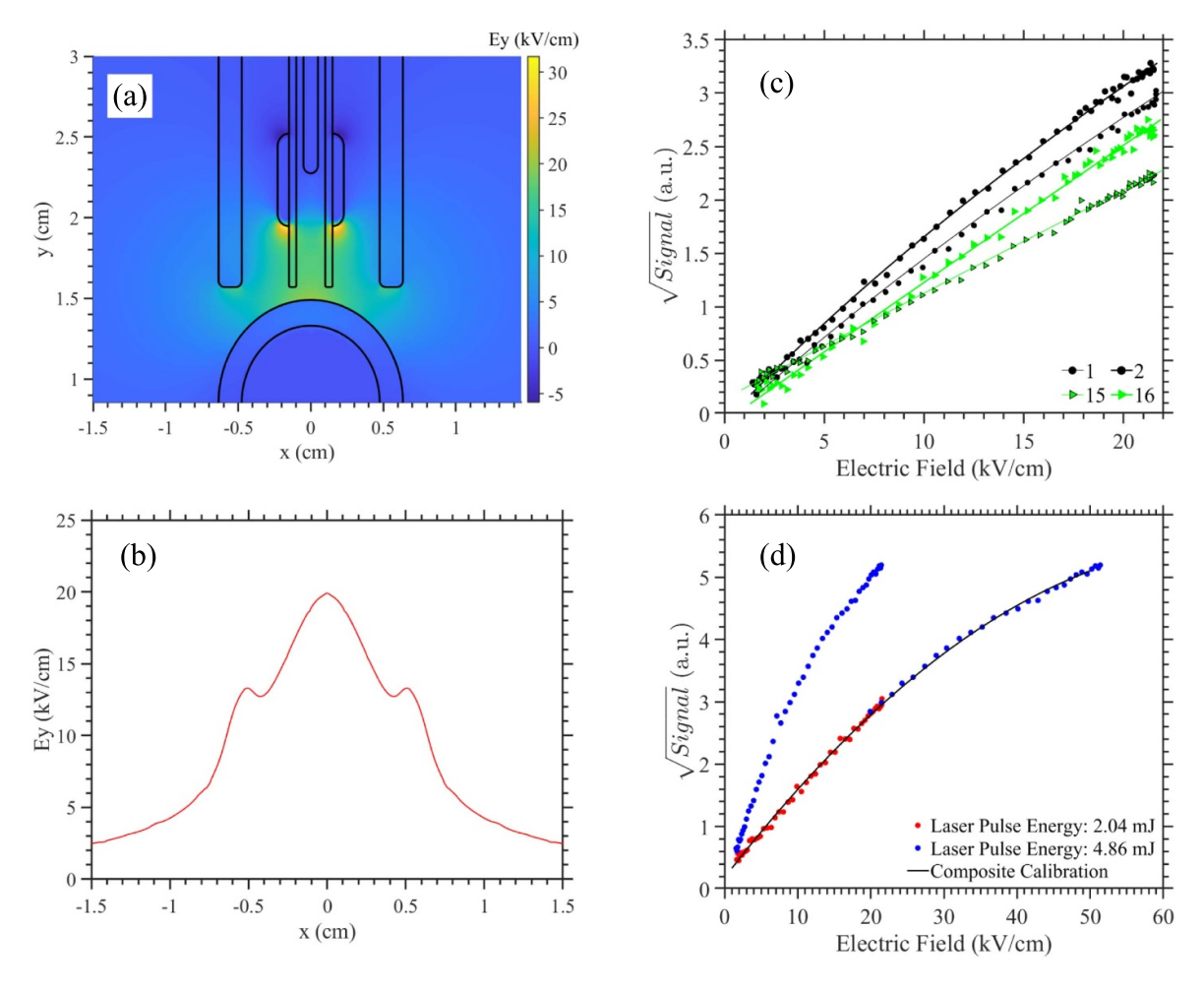


**Figure 5.** (a) Laplacian field distribution for a 10 kV voltage applied to both electrodes of the plasma jet assembly; (b) vertical electric field profile along the laser beam (tangent line to the Macor surface); (c) typical Laplacian field EFISH calibration curves measured in a sub-breakdown voltage pulse, at different locations along the Macor surface; (d) typical composite calibration curve used for the calibration data extrapolation.

 $\sqrt{S(E_1,I_1)}$  when  $E_2I_2 = E_1I_1$ , such that the PMT signal scales as the product of the electric field and laser intensity. This relationship was used to scale the higher laser intensity curve to the higher electric field values, as shown in figure 5(d). A similar approach was used in our previous work [18], where the composite calibration data were obtained for two different pressures, using the following scaling relationship,  $\sqrt{S(E_2,P_2)} = \sqrt{S(E_1,P_1)}$  when  $E_2P_2 = E_1P_1$ .

The calibration procedure used in the present work does not entirely remove the uncertainty in the electric field measured at the beam focal point. Recently it has been shown [14] that the EFISH signal generated in a plasma probed by a focused laser beam depends not only on the electric field, but also on the extent and shape of the electric field spatial distribution along the beam. At the present conditions, both the beam Rayleigh range,  $z_R = \frac{\pi w_0^2}{\lambda} \approx 30$  mm, and the coherence length  $L_c = \frac{\pi}{|\Delta k|} \approx 63$  mm  $> z_R$  (where  $|\Delta k| \approx 0.5$  cm<sup>-1</sup> is the wave vector mismatch), are much greater than the extent of the plasma in the direction of the beam, estimated from the optical emission,  $L \approx 5$  mm, such that  $L \ll z_R$ ,  $L_c$ , and the plane wave approximation can be used. On the other hand, the

spatial resolution of the present measurements (in the direction of the laser beam) is relatively low, such that the signal is controlled by the electric field integrated along the line of sight. Therefore the Laplacian field calibration would yield the accurate peak electric field value in the plasma only if its spatial distribution is the same as that produced in the plasma jet. This is the most significant uncertainty of the present measurements.

Assigning the direction to the electric field vector components may be challenging, since in some cases it cannot be determined unambiguously from the EFISH data. For this, we relied on the charge transport in the externally applied electric field, as well as the comparison with the simulations, discussed in the companion paper [16]. The basic assumption is that the electric field in the decaying plasma after the voltage on the high-voltage electrode is turned off is controlled by the residual surface charge, which generates the polarization field directed opposite to the externally applied field. This rationale is used to determine the sign of the vertical and horizontal electric field components after the field reversal during the IW arrival and decay, discussed in section 3. In cases when the field reversal occurs at longer time delays

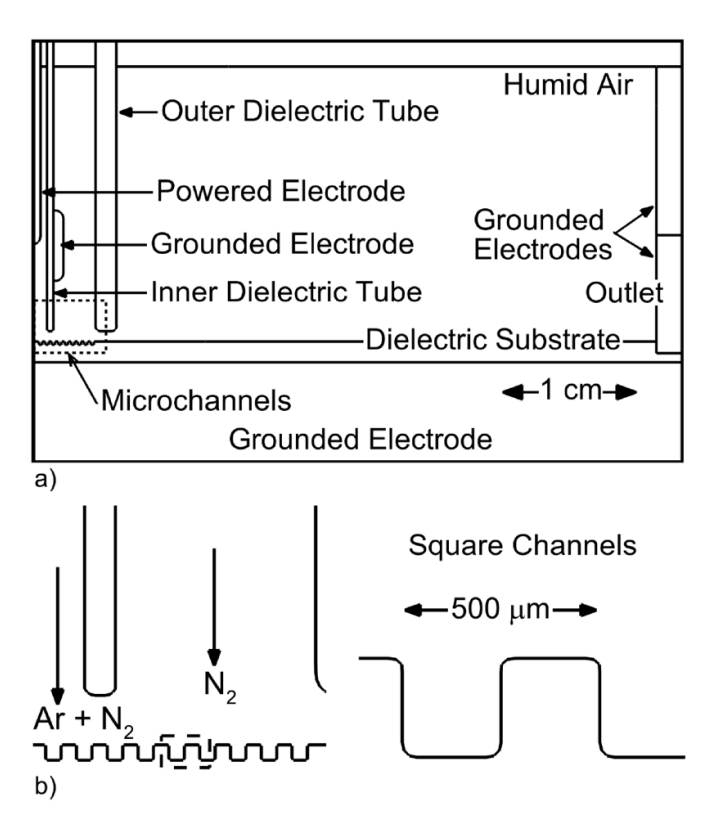


Figure 6. Schematic of the computational domain for simulations: (a) entire computational domain, (b) enlargement of microchannels.

after the wave arrival, and therefore is not detected directly, the direction of the residual electric field before the arrival (opposite to that of the peak electric field in the wave) is determined based on the same argument. This assumption has been verified by the comparison with the simulation predictions.

## 2.2. Kinetic model

A selection of the experiments on the APPJ treatment of microchannels were simulated using the 2D plasmahydrodynamics model, nonPDPSIM. The model is described in detail in [19]. Briefly, nonPDPSIM is a plasma hydrodynamics model executed on an unstructured mesh. Continuity equations for charged particles with the simultaneous solution of Poisson's equation for electric potential are implicitly integrated in time, while taking into account the surface and volumetric charging of solid materials. After an integration timestep (whose duration is dynamically chosen) of charged species transport, continuity equations for neutral species and electron temperature are updated using the same timestep. Rate coefficients as a function of average electron energy (or electron temperature) are produced from solutions of the stationary Boltzmann's equation for the electron energy distribution. Radiation transport, photoionization and photoelectron emission are addressed using a Green's function propagator. Neutral particle transport is addressed using a modified compressible form of Navier-Stokes (NS) equations, which produces a single fluid flow field. Neutral species have this average advective velocity while additionally diffusing within the flow field.

For the simulations, the 2D geometry shown in figure 6 is used. The central nozzle flows a gas mixture of  $Ar/N_2/O_2/H_2O = 0.9/0.1/10^{-5}/10^{-5}$ , with a gas shield of  $N_2$  flowing into humid air. A more detailed description of the model and reaction mechanism, and more extensive discussion of simulation results are in the companion paper [16].

# 3. Results and discussion

A collage of phase-locked, ensemble-averaged images of the plasma optical emission at different moments of time after breakdown are shown in figure 7. The images are taken over the microchannel array surface with empty channels (left column) and channels filled with water (right column). In both cases, it is readily apparent that the plasma is propagating as a surface ionization wave (SIW). When the microchannels are empty, the plasma clearly 'hops' across the channels, leaving the well-defined gaps in the optical emission, such that almost no emission is generated inside the channels (see figure 7, left column). The hopping occurs only outside of the incident plasma jet, while the optical emission fills the channels within the jet. Qualitatively, this is consistent with the behavior predicted in the recent simulations of SIW propagation in air [8], where it was attributed to the shielding of ionization radiation of O<sub>2</sub> by the opaque channel walls. When the channels are filled with water, the plasma tends to 'hug' the surface, that is

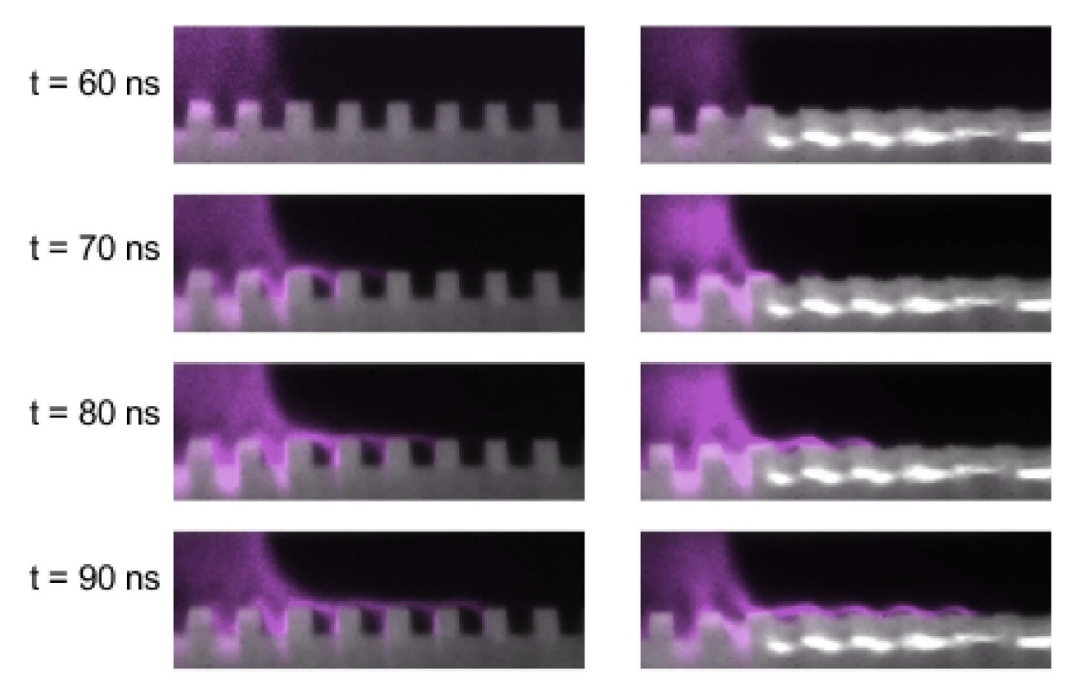
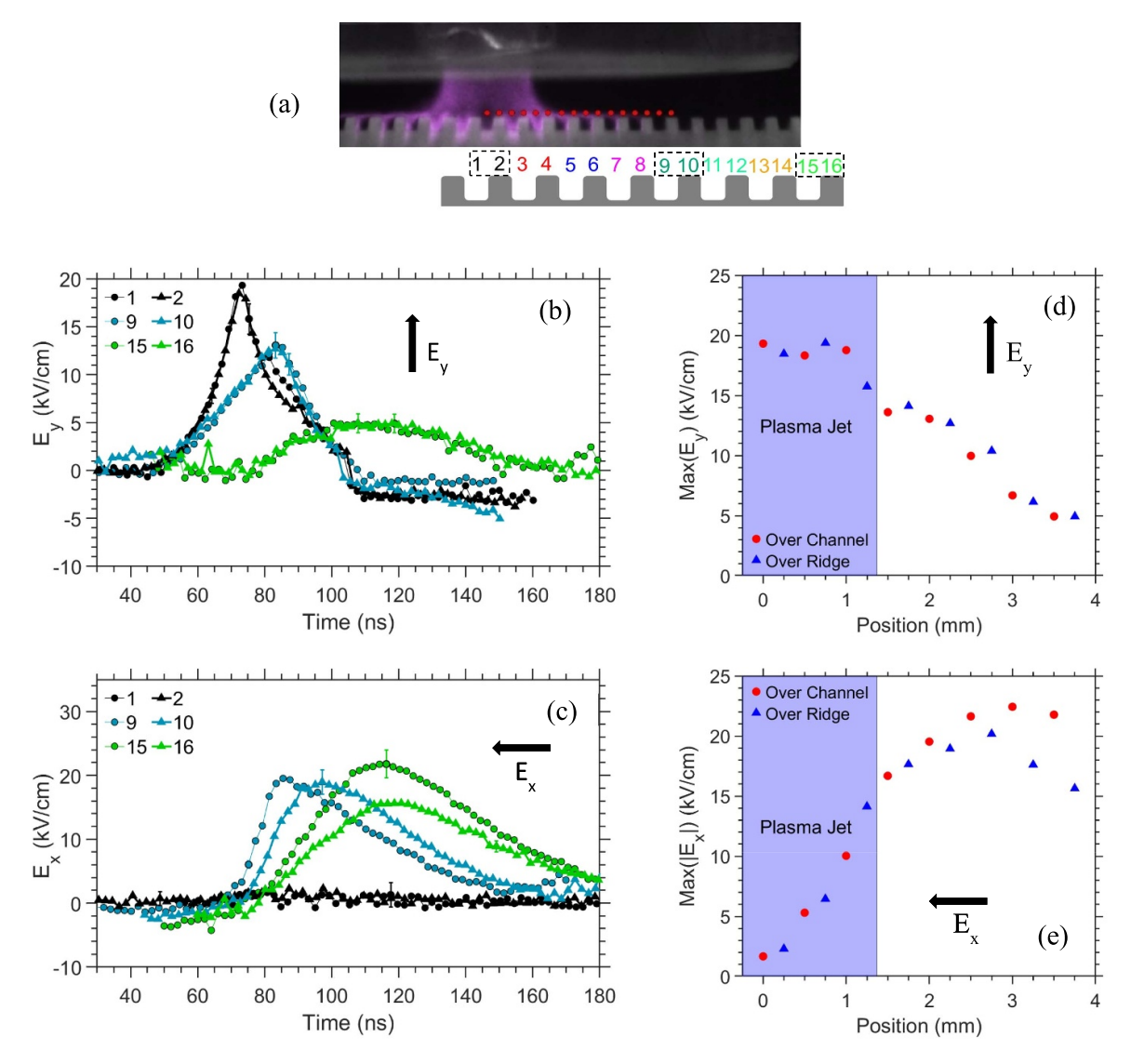


Figure 7. Plasma optical emission images at different moments of time, illustrating the surface ionization wave propagation along the microchannel surface. Left: empty channels, right: channels filled with water. The reference point in time is the same as in figure 2.

propagates much closer to it, although smaller gaps between the surface and the plasma emission are still evident. Note that in this case the jet effluent displaces the water from the channels within the jet, such that they become nearly empty (see figure 7, right column). The movies assembled from the individual images such as shown in figure 7, provided in the supporting information, give a more detailed illustration of these effects.

The present measurements of the spatio-temporal distributions of the electric field in the plasma jet are divided into the three separate series of data: (i) measurements over the microchannel surface with dry channels, taken by scanning the laser beam along the surface at the same laser beam height; (ii) measurements over the same dry surface, but taken at different laser beam heights, i.e. inside the channels and over the ridges between the channels, as shown in figure 3; and (iii) measurements over the surface when the channels are filled with water, also obtained by scanning the laser beam along the surface at the same laser beam height. The results of these three series of measurements are summarized in figures 8-10, respectively. A cartoon schematic of the laser beam locations, overlapped with the plasma emission images, is shown in every figure for reference. In these figures, the reference point in time (t = 0)is the same as that in figure 2 and corresponds to the breakdown moment in the plasma jet assembly. In each case, the data were taken at 16 different locations along the microchannel surface, 8 over the channels (inside the channels) and 8 over the ridges. For each location, both the vertical and horizontal time-resolved field components,  $E_v$  and  $E_x$ , were measured separately, by rotating the polarizer places before the PMT detector. The field measurements in the plasma at each spatial location (both vertical and horizontal components) are matched with the respective Laplacian field measurements, for the absolute calibration. Thus, each of the three data series has 32 time-resolved, absolute data sets. Figures 8–10 show only several representative data sets, chosen to illustrate the dominant trends. In addition, the data taken at every spatial location are plotted in figures S1–S3 of the supporting information and are available upon request.

From figure 8, it is readily apparent that the plasma propagates away from the impinging jet as a SIW, as expected. The vertical electric field  $(E_v)$  is highest on the centerline of the jet (location 1), where the horizontal field  $(E_x)$  is near zero (below detection limit, see figures 8(b) and (c)). As the plasma propagates along the microchannel surface away from the jet (locations 1–16), the peak value of  $E_{\nu}$  gradually decreases while that of  $E_x$  increases, indicating that the horizontal field may play an increasingly more important role in the SIW propagation away from the incident plasma jet. There is essentially no detectable difference between the vertical field waveforms measured at the adjacent locations (locations 1-2, 9-10, and 15-16, over a channel and over an adjacent ridge), as can be seen from figure 8(b). There is a relatively small but detectable difference between the horizontal field waveforms at the respective adjacent locations, which becomes more pronounced further away from the impinging jet (see figure 8(c)). The horizontal field over the channels rises more rapidly compared to that over the adjacent ridges further away from the jet. The peak values of  $E_v$  and  $E_x$  vs. the distance from the jet centerline are plotted in figures 8(d) and (e), illustrating further the variation of the electric field components along the IW path. It is evident that the difference between the electric field measured over

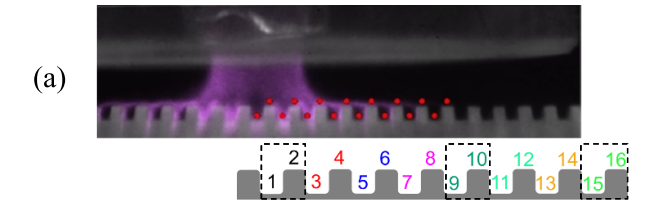


**Figure 8.** Summary of the electric field measurements over the microchannel surface with empty (dry) channels, taken at the same laser beam height: (a) schematic of the measurement locations (1–16), overlapped with a plasma emission image; (b), (c) time-resolved field components,  $E_y$  and  $E_x$ , respectively, at select locations; (d), (e) peak values of  $E_y$  and  $E_x$ , respectively, plotted vs. distance along the surface. Odd-numbered locations and red data points correspond to the measurements over the channels, even numbers and blue points are the measurements over the ridges between the channels. The approximate extent of the plasma jet is indicated by a purple-shaded area.

the channels and over the ridges is relatively minor, such that the presence of the channels does not affect significantly the electric field distribution outside the channels.

This trend changes in the second series of measurements, when the electric field is measured inside the channels and over the ridges, as shown in figure 9(a). In this case, the difference between the peak  $E_y$  values measured in the channels and adjacent ridges becomes detectable (see figure 9(b)). In addition, peak  $E_x$  values measured in the channels are significantly higher compared to those measured over the respective ridges (by up to a factor of 2, from  $\approx$ 18 kV cm<sup>-1</sup> to  $\approx$ 34 kV cm<sup>-1</sup>, see figure 9(c), and from  $\approx$ 20 kV cm<sup>-1</sup> to  $\approx$ 40 kV cm<sup>-1</sup>, see figures S2(d) and (e)). This effect is illustrated further in figure 9(e). The horizontal electric field in the channels located further away from the plasma jet decays slowly and eventually reverses direction, such that the residual electric field before

the pulse is no longer near zero and directed away from the jet (see figure 9(c)). It can be seen that the residual electric field decreases to near detection limit when the wave approaches the measurement location, and then increases again, indicating the change in the sign of the horizonal field component. In some of the channels, the same effect is also observed for the vertical electric field (see figure 9(b)). Thus, there is a strong residual electric field inside the channels remaining after the pulse. This indicates that the transport of the charged species between the plasma and the channels is obstructed, such that the charges accumulated on the dielectric surface are not neutralized by the opposite polarity charges coming from the plasma. Also, the rise time for the vertical electric field in the channels away from the plasma jet,  $E_{v}$ , is now longer compared to that at the two neighboring ridges (see figure 9(b)), although the horizontal field in the channels still rises faster (see figure 9(c)).



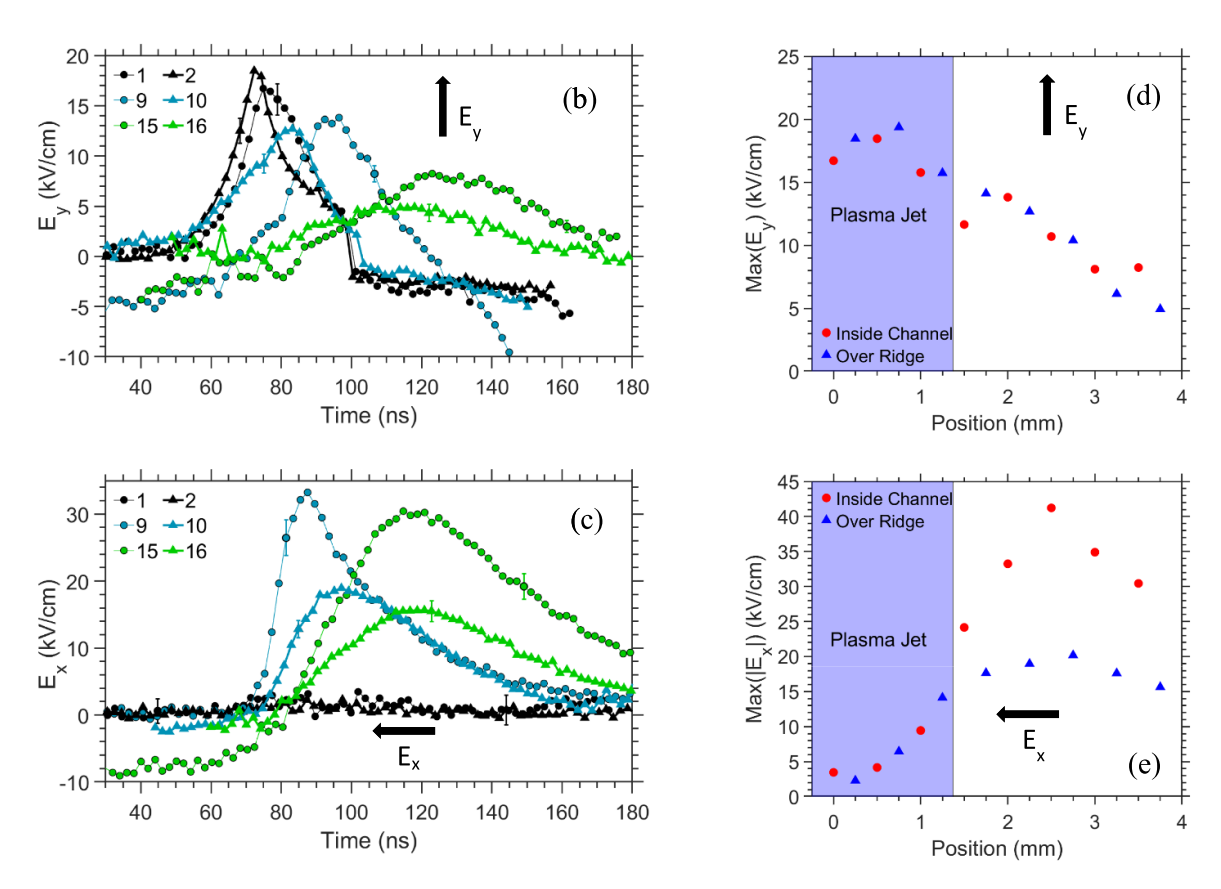


**Figure 9.** Summary of the electric field measurements over the microchannel surface with dry channels, taken at different laser beam heights: (a) schematic of the measurement locations (1–16), overlapped with a plasma emission image; (b), (c) time-resolved field components,  $E_y$  and  $E_x$ , respectively, at select locations; (d), (e) peak values of  $E_y$  and  $E_x$ , respectively, plotted vs. distance along the surface. Odd-numbered locations and red data points correspond to the measurements inside the channels, even numbers and blue points are the measurements over the ridges between the channels. The approximate extent of the plasma jet is indicated by a purple-shaded area.

The results of the electric field measurements, when the microchannels are filled with water, plotted in figure 10, are somewhat similar to the first series of data, shown in figure 8. Although the difference between the waveforms measured over the channels and ridges is more pronounced, no significant residual field after the discharge pulse is detected. It is also apparent that the peak vertical electric field decays much slower with the distance from the jet (see figures 10(b) and (d)), while the rise of the peak horizontal field with distance is noticeably faster (see figures 10(c) and (e)). This suggests that the IW traveling along the microchannel surface with water-filled channels has a lower attenuation rate and would propagate over a longer distance.

The SIW trajectories for these three cases, where the wave arrival is defined as the time moment when the vertical field reaches the peak value, are shown in figure 11. The most significant difference between Case 2 and the other two cases is a consistent time lag between the moments when  $E_y$  peaks inside the channels, compared to that at the two adjacent ridges. This can be interpreted as the evidence of the 'reverse wave', directed from the ridge further away from the jet into the channel. A major difference of Case 3 from the other two is that the wave propagates noticeably faster over the channels filled with water. This is most likely caused by the electric field enhancement near the water surface due to its significantly high dielectric constant, compared to Macor ceramic ( $\varepsilon_w \approx 80$  vs.  $\varepsilon_c \approx 6$ ). This result is also consistent with the recent modeling predictions [8], where increasing the dielectric constant of the surface resulted in higher velocity of the surface streamer propagation.

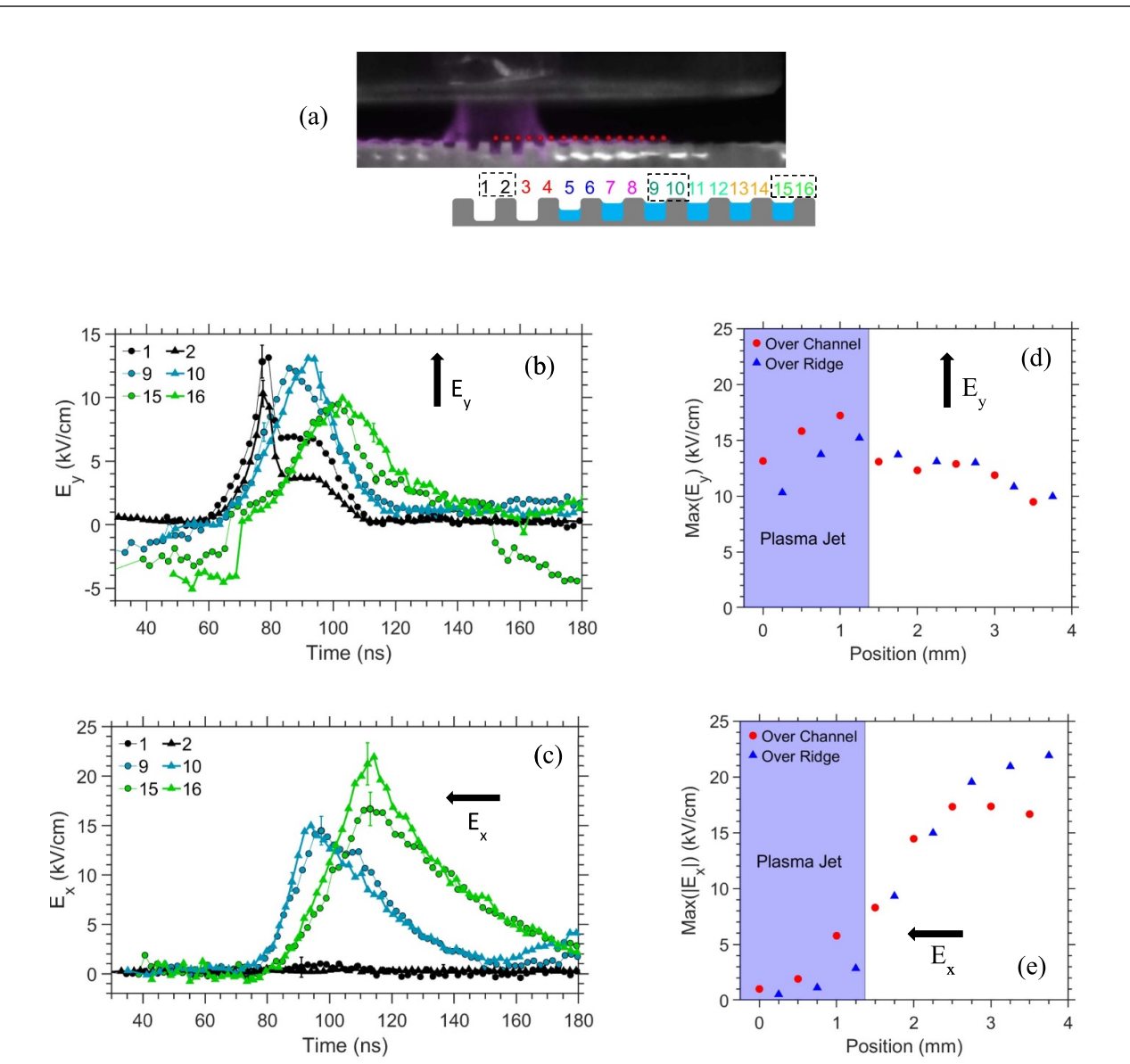


**Figure 10.** Summary of the electric field measurements over the microchannel surface with channels filled with water, taken at the same laser beam height: (a) schematic of the measurement locations (1–16), overlapped with a plasma emission image; (b), (c) time-resolved field components,  $E_y$  and  $E_x$ , respectively, at select locations; (d), (e) peak values of  $E_y$  and  $E_x$ , respectively, plotted vs. distance along the surface. Odd-numbered locations and red data points correspond to the measurements over the water-filled channels, even numbers and blue points are the measurements over the ridges between the channels. The approximate extent of the plasma jet is indicated by a purple-shaded area.

The hopping of the plasma waves across the surface, and reverse IWs that are strongly indicated by the plasma emission imaging, are corroborated by the computational modeling for both dry and water filled channels. Computed electron densities are shown in figure 12 for SIW propagation over dry and water filled channels. The APPJs were initiated as a negative polarity discharge. The images are of the middle of the chain of microchannels on the right side of the prior experimental images, and so propagate from left to right. In both cases, maximum electron densities are in excess of  $10^{14}$  cm<sup>-3</sup>, and propagate as a series of hops. The propagation over the dry channels occurs in repetitive stages. The cycle begins with the plasma propagating as a negative polarity SIW on the ridge of the previous channel (0 ns), indicated by the negative space charge at its leading edge. When reaching the edge of the ridge,

a negative polarity bulk IW is launched across the channel, directed towards the electric field enhancement at the vertex of the next ridge (0.5 ns). The bulk IW leaves the interior of the channel largely unexposed to plasma. When the dielectric vertex is charged by the incident IW, negative polarity SIWs are launched across the ridge to the right and down the interior surface of the channel (0.7, 1.0 ns), the latter partially filling the channel with the plasma (1.0, 1.5 ns). At this time (0.7, 1.0 ns), a reverse, positive polarity bulk IW is launched back across the channel to the previous ridge, following the preionized path of the incident IW. The majority of the ionization occurring in the plasma over the channel occurs by the reverse IW (1.5 ns).

A similar sequence of events occurs during the IW propagation over water filled channels, although with more clearly

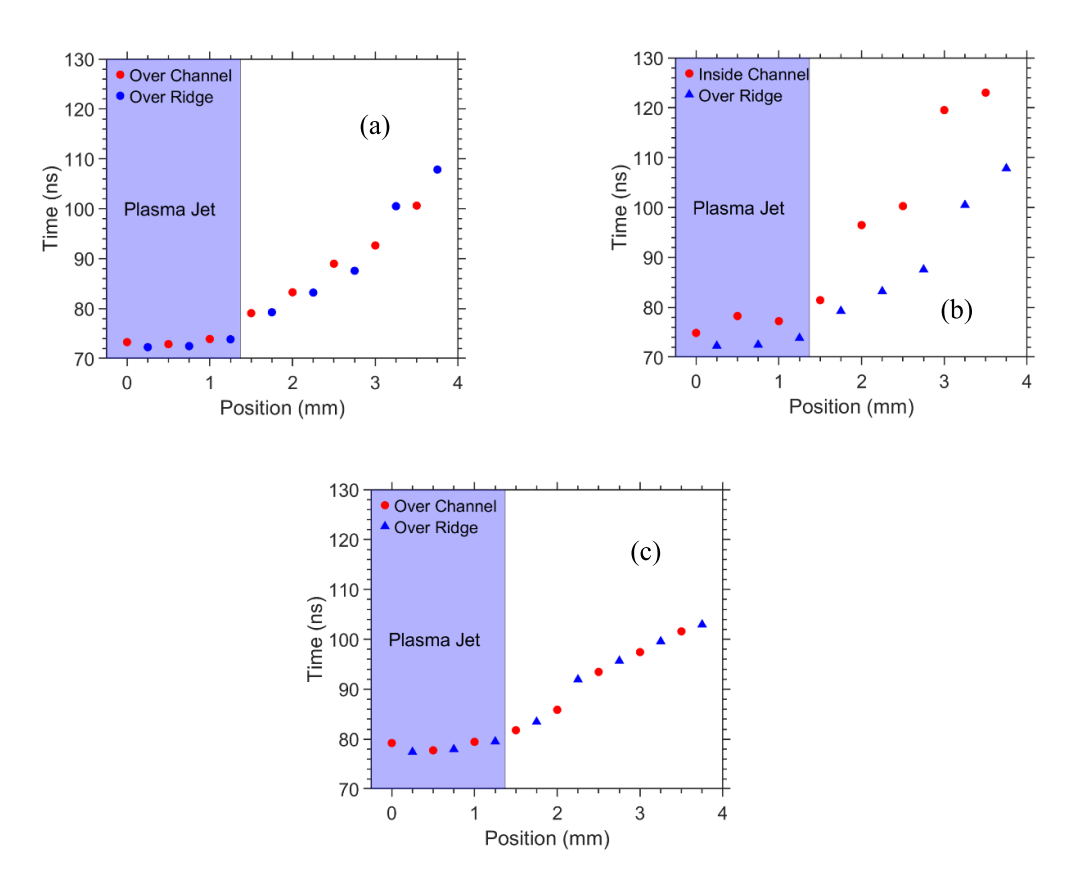


**Figure 11.** Comparison of the ionization wave propagation timing at the conditions of figures 8-10, based on the time to reach the peak  $E_y$  value at different measurement locations: (a) dry channels, same laser beam height (see figure 8) (b) dry channels, different laser beam heights (see figure 9) (c) channels filled with water, same laser beam heights (see figure 10). Red symbols correspond to the measurements inside or over the channels, blue symbols are the measurements over the ridges between the channels.

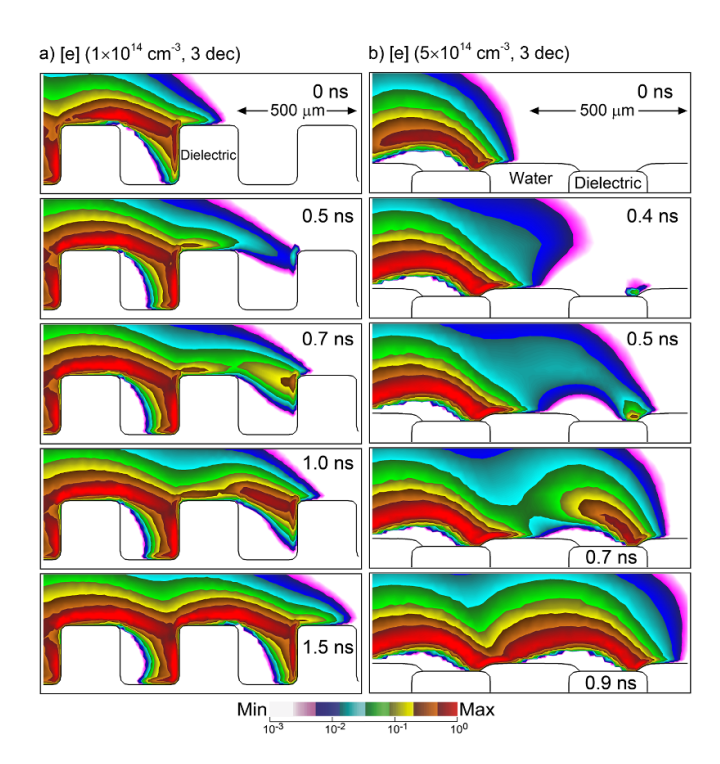


**Figure 12.** Computed electron densities for propagation of ionization waves over (a) dry and (b) water-filled channels. The densities are plotted on a 3-decade log-scale with the maximum value indicated. The ionization waves propagate as a series of forward (negative) and reverse (positive) waves, hopping across the surface.

defined hops. Here, the electric field enhancement occurs at the leading edge of the meniscus of the water filling the channel. The intersection of the water ( $\varepsilon_{\rm w}=80$ ), ceramic ridge ( $\varepsilon_{\rm c}=6$ ) and plasma ( $\varepsilon_p = 1$ ) creates a triple-point like structure that additionally intensifies the local electric field. A forward negative polarity IW is launched from the leading edge of the prior water filled channel (0 ns) and is focused towards the electric field enhancement at the leading edge of the present water filled channel (0.4, 0.5 ns). The duration of this plasma interaction with the water is shorter than the dielectric relaxation time of the distilled water, such that the surface of the water charges. This charging launches a reverse positive bulk IW following the preionized path of the incident wave (0.5, 0.7 ns), producing the majority of the ionization bridging the water and ridges (0.9 ns). The IWs largely hop across the dielectric ridges of the channels, from leading edge to leading edge of the water surface. More detailed discussion of results of the simulations are given in the companion paper [16].

The comparison of figures 11(a) and 12(a), as well as figures 11(c) and 12(b), indicates that the wave speed predicted in the simulations exceeds the experimental values by a factor of 4–5. This is most likely due to the difference in the discharge geometry. In the experiment, the SIW is generated by an axisymmetric plasma jet impinging on a microchannel surface with a significantly larger radius of curvature, resulting in a nearly circular initial IW front propagating in three dimensions. In the simulations, the wave is assumed to be propagating in a quasi-2-D rectangular geometry, such that the IW front is plane. As discussed in the companion paper [16], obtaining the comparable IW characteristics in the simulations requires increasing the voltage on the electrode by a factor of 1.5–2, which also results in a higher predicted IW speed.

# 4. Summary

The electric field measurements in the SIW s propagating over a microchannel array surface, with channels being empty or filled with distilled water indicate the following dominant trends. First, the effect of the electric field enhancement is largely localized within the channels, and the difference in the field components measured above the channels and the adjacent ridges is relatively modest. Second, the horizontal field,  $E_x$ , inside the channels is strongly enhanced and exceeds considerably the respective field component measured at the adjacent ridges, by up to a factor of 2. Third, the residual field inside the channels (after the pulse) persists for a long time and is detected before the discharge pulse, indicating the obstructed charge transfer between the plasma and the channels. Fourth, the vertical electric field inside the channels,  $E_{\nu}$ , has a longer rise time compared to that at the two adjacent ridges, suggesting the local reversal of the IW propagation direction (from the further ridge into the channel). This is consistent with the plasma emission images, which demonstrate that the IW 'hops' over the empty channels and propagates into the channels only after the 'flashover' between the adjacent ridges. Finally, the wave speed measured over the array channels filled with water is significantly higher, by approximately 50%, most likely due to the higher effective dielectric constant of the surface.

The use of ps EFISH generation for the electric field characterization in the SIW, although insightful, also illustrates the limitations of the diagnostic. Most significantly, the spatial resolution of a single-beam EFISH in the direction of the laser beam is low, which introduces an uncertainty in the measurements, which is difficult to quantify without the prior knowledge of the electric field distribution. The use of ps SEEFISH employing two crossed beams would help resolve this difficulty, at the cost of a precipitous loss in sensitivity, as shown in our previous work [15]. However, recent fs SEEFISH measurements in a ns pulse discharge in air [20] indicate that there is considerable potential of this diagnostics for the spatially-resolved electric field measurements in atmospheric pressure plasmas, due to much higher peak intensity and higher pulse repetition rate of the pump laser.

The present measurements do not show evidence of the dramatic enhancement of the electric field in the immediate vicinity of the dielectric surface (Macor ceramic or water), predicted by the modeling calculations [7, 18]. This is most likely due to the limited spatial resolution of the present approach,  $\sim 100 \ \mu \text{m}$  compared to the  $\sim 10 \ \mu \text{m}$  scale predicted in the simulations. It is also very likely that the electric field at the water surface may be even higher than that predicted in the plasma. Probing it would require reflecting the pump laser beam off the water surface, as has been done recently in surface-enhanced fs EFISH and SHG experiments [21]. In particular, these measurements indicate that the electric field measured in the interfacial layer of the water surface has the direction opposite to the applied electrostatic field. This result suggests that continuum models of the interfacial shielding, even without plasma, may not reflect the structural complexity on the molecular level, and demonstrates the need for the further plasma-water interface diagnostic and modeling effort.

## Data availability statement

All data that support the findings of this study are included within the article (and any supplementary files).

# **Acknowledgments**

The support of US Department of Energy Center for Plasma Interaction with Complex Interfaces is gratefully acknowledged. This work was supported by the Department of Energy Office of Fusion Energy Sciences (DE-SC0020232), the Army Research Office MURI program (W911NF-20-1-0105) and the National Science Foundation (CBET-2032604).

## **ORCID iDs**

### References

- [1] Gibalov V I and Pietsch G J 2012 Dynamics of dielectric barrier discharges in different arrangements *Plasma Sources* Sci. Technol. 21 024010
- [2] Lu X, Naidis G V, Laroussi M and Ostrikov K 2014 Guided ionization waves: theory and experiments *Phys. Rep.* 540 123
- [3] Wang D and Namihira T 2020 Nanosecond pulsed streamer discharges: II. Physics, discharge characterization and plasma processing *Plasma Sources Sci. Technol.* 29 023001
- [4] Viegas P, Slikboer E, Bonaventura Z, Guaitella O, Sobota A and Bourdon A 2022 Physics of plasma jets and interaction with surfaces: review on modelling and experiments *Plasma Sources Sci. Technol.* 31 053001
- [5] Winters C, Petrishchev V, Yin Z, Lempert W R and Adamovich I V 2015 Surface charge dynamics and OH and H number density distributions in near-surface nanosecond pulse discharges at a liquid/vapor interface J. Phys. D: Appl. Phys. 48 424002
- [6] Simeni Simeni M, Baratte E, Zhang C, Frederickson K and Adamovich I V 2018 Electric field measurements in nanosecond pulse discharges in air over liquid water surface Plasma Sources Sci. Technol. 27 015011
- [7] Konina K, Kruszelnicki J, Meyer M E and Kushner M J 2022 Surface ionization waves propagating over non-planar substrates: wavy surfaces, cut-pores and droplets *Plasma* Sources Sci. Technol. 31 115001
- [8] Marskar R and Meyer H K H 2023 A kinetic Monte Carlo study of positive streamer interaction with complex dielectric surfaces *Plasma Sources Sci. Technol.* 32 085010
- [9] Dogariu A, Goldberg B M, O'Byrne S and Miles R B 2017 Species-independent femtosecond localized electric field measurement *Phys. Rev. Appl.* 7 024024
- [10] Goldberg B M, Reuter S, Dogariu A and Miles R 2019 1D time evolving electric field profile measurements with sub-ns resolution using the E-FISH method Opt. Lett. 44 3853
- [11] Orr K, Tang Y, Simeni Simeni M, van den Bekerom D and Adamovich I V 2020 Measurements of electric field in an atmospheric pressure helium plasma jet by the E-FISH method *Plasma Sources Sci. Technol.* 29 035019

- [12] Lepikhin N D, Luggenhölscher D and Czarnetzki U 2021 Electric field measurements in a He:N<sub>2</sub> nanosecond pulsed discharge with sub-ns time resolution *J. Phys. D: Appl. Phys.* 54 055201
- [13] Huang B, Zhang C, Zhu W, Lu X and Shao T 2021 Ionization waves in nanosecond pulsed atmospheric pressure plasma jets in argon *High Volt*. 6 665
- [14] Chng T L, Starikovskaia S M and Schanne-Klein M-C 2020 Electric field measurements in plasmas: how focusing strongly distorts the E-FISH signal *Plasma Sources Sci. Technol.* 29 125002
- [15] Raskar S, Orr K, Adamovich I V, Chng T L and Starikovskaia S M 2022 Spatially enhanced electric field induced second harmonic (SEEFISH) generation for measurements of electric field distributions in high-pressure plasmas *Plasma Sources Sci. Technol.* 31 085002
- [16] Konina K, Raskar S, Adamovich I V and Kushner M J Atmospheric pressure plasmas interacting with wet and dry microchannels: reverse surface ionization waves *Plasma* Sources Sci. Technol. 33 015002
- [17] van Gessel A F H, Alards K M J and Bruggeman P J 2013 NO production in an RF plasma jet at atmospheric pressure J. Phys. D: Appl. Phys. 46 265202
- [18] Orr K, Yang X, Gulko I and Adamovich I V 2020 Formation and propagation of ionization waves during Ns pulse breakdown in plane-to-plane geometry *Plasma Sources Sci. Technol.* 29 125022
- [19] Norberg S A, Johnsen E and Kushner M J 2015 Formation of reactive oxygen and nitrogen species by repetitive negatively pulsed helium atmospheric pressure plasma jets propagating into humid air *Plasma Sources Sci. Technol.* 24 035026
- [20] Vorenkamp M, Steinmetz S A, Chen T Y, Ju Y and Kliewer C J 2023 Suppression of coherent interference to electric field induced second harmonic (E-FISH) signals for the measurement of electric field in mesoscale confined geometries Opt. Lett. 48 1930
- [21] Ray K K, Limaye A, Ng K C, Saha A, Shin S, Biswas B, Gaigeot M-P, Pezzotti S, Willard A P and Allen H C 2023 Second-harmonic generation provides insight into the screening response of the liquid water interface *J. Phys. Chem.* C 127 14949